

Pressure profiles of plasmas confined in the field of a magnetic dipole

Matthew S Davis¹, M E Mael¹ Darren T Garnier¹ and Jay Kesner²

¹ Department of Applied Physics and Applied Mathematics Department, Columbia University, New York, NY, 10027, USA

² Plasma Science and Fusion Center, MIT, Cambridge, MA, 02139, USA

Received 13 January 2014, revised 18 June 2014

Accepted for publication 3 July 2014

Published 6 August 2014

Abstract

Equilibrium pressure profiles of plasmas confined in the field of a dipole magnet are reconstructed using magnetic and x-ray measurements on the levitated dipole experiment (LDX). LDX operates in two distinct modes: with the dipole mechanically supported and with the dipole magnetically levitated. When the dipole is mechanically supported, thermal particles are lost along the field to the supports, and the plasma pressure is highly peaked and consists of energetic, mirror-trapped electrons that are created by electron cyclotron resonance heating. By contrast, when the dipole is magnetically levitated losses to the supports are eliminated and particles are lost via slower cross-field transport that results in broader, but still peaked, plasma pressure profiles.

Keywords: nuclear fusion, magnetic dipole, pressure profiles

(Some figures may appear in colour only in the online journal)

1. Introduction

The relationship between the pressure profile and the toroidal ring current has long been important to the study of equilibria and dynamics of planetary magnetospheres [1, 2]. High pressure plasma and the resulting ring current in space are measured by taking the curl of *in situ* magnetic field measurements [3], using ground-based magnetic measurements [4], low-altitude satellite measurements [5], and high-altitude particle measurements [6]. These spacecraft observations of high beta plasmas confined in planetary magnetospheres motivated the dipole confinement concept [7–10]. Plasma within planetary magnetospheres have peaked density and pressure profiles [11–14], and the plasma pressure and ring current increase during geomagnetic storms caused by fluctuations of the solar wind [15].

In the levitated dipole experiment (LDX) [16, 17], shown in figure 1, a 565 kg superconducting coil is magnetically levitated inside a 5 m diameter vacuum vessel. Calculations of plasma equilibrium in LDX show stability at peak plasma pressure that is ten times larger than the local magnetic pressure [18]. Levitating the coil eliminates particle losses along the magnetic field lines to material supports. The plasmas are heated by electron cyclotron resonance heating (ECRH) with the application of up to 27 kW of power distributed in

4 frequencies, 2.45 GHz (4 kW), 6.4 GHz (3 kW), 10.5 GHz (10 kW) and 28 GHz (10 kW).

Levitated plasmas on LDX are predicted to reach pressure profiles that are limited by marginal stability to the magnetohydrodynamic (MHD) interchange mode [11, 18, 19]

$$\delta(pV^\gamma) = 0 \quad (1)$$

where p is the plasma pressure, V is the differential flux-tube volume ($V \equiv \oint dl/B$ with the integration along the magnetic field and B the magnetic field strength), and γ is the ratio of specific heats ($\gamma = 5/3$). In addition to being a marginal stability point, equation (1) describes a pressure profile that is invariant to interchange motion. Thus, a plasma at the marginal stability point can undergo an adiabatic mixing of plasma filled flux-tubes without changing its pressure profile. A similar invariant profile is adopted by the flux-tube integrated density

$$\delta(nV) = 0 \quad (2)$$

where n is the plasma density. Thus, a plasma can undergo low-frequency convective mixing without changing its density profile. These profiles also represent stationary states of space-weather dynamics [20] for the special case when driven mixing of magnetospheric plasma does not alter plasma profiles.

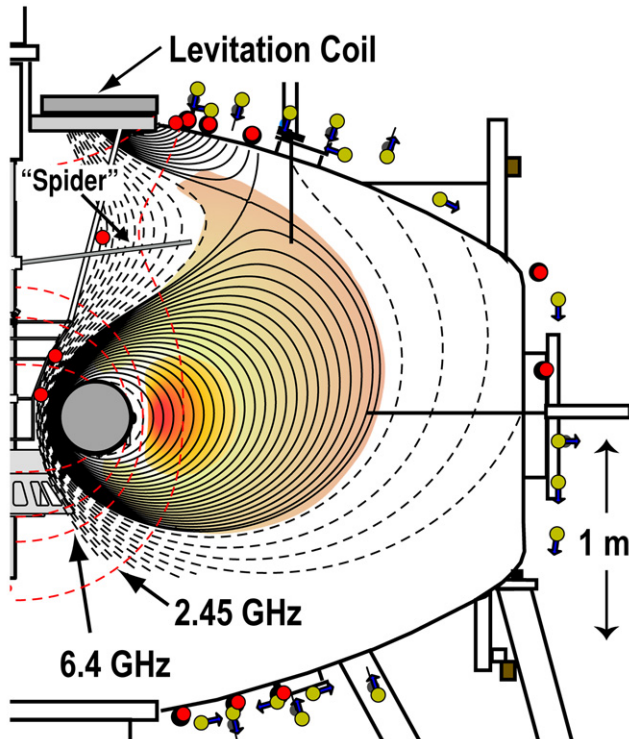


Figure 1. A schematic drawing of the LDX experiment. Closed magnetic field lines are illustrated with solid black contours; open field lines are shown with dashed black contours. The fundamental ECRH resonance surfaces for the 2.45 GHz source and the 6.4 GHz source are illustrated with thick dashed lines. Locations of the azimuthal magnetic flux loops are shown by the red dots. Locations and orientations of the poloidal field coils are shown by the blue arrows with yellow dots.

Gyrokinetic simulations [21] and theory [22] provide an explanation for the turbulent self-organization of the plasma driven towards these stationary profiles, which are states of minimum entropy production [23].

In the dipole geometry, $\mathbf{B} = \nabla\varphi \times \nabla\psi$, and the axisymmetric magnetic field is described in terms of the toroidal angle, φ , and magnetic flux, ψ , which varies inversely with the equatorial radius, $\psi \sim 1/R$. The equatorial magnetic field strength has power-law scaling, $B \sim \psi^3 \sim 1/R^3$, and the differential flux-tube volume increases rapidly, $V \sim R^4 \sim \psi^{-4}$. Because V varies radially as a power-law, the invariant profiles represented by equations (1) and (2) are often represented with power-law models. Gold [11] used a power-law formulation of the equilibrium pressure profile to evaluate magnetospheric stability, and Krasheninnikov *et al* [24] used a power-law formulation to demonstrate that plasma confined by a point magnetic dipole remains stable at arbitrary beta. Reconstructions of the quiet time magnetospheric ring current using satellite measurements of energetic particles also found power-law dependences [25], and similar profiles were shown to result during storm-time enhancements of the ring current [26].

Centrally-peaked power-law profiles of plasma pressure and density were observed in previous studies of LDX. When the dipole was mechanically supported, the pressure profile was magnetically reconstructed and found to vary as $p \sim \psi^{4g}$

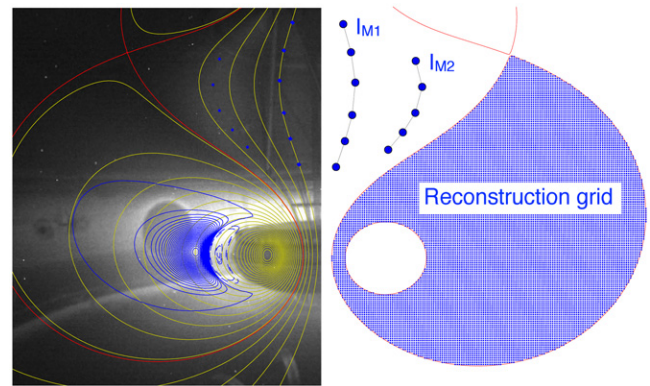


Figure 2. Left: a grayscale visible light image of a plasma shot with magnetic field lines overlaid in yellow, separatrix in red, and current density contours in blue. Right: the reconstruction grid. Plasma currents (shown as blue dots) are placed on grid nodes between the separatrix (outer red contour) and the limited innermost flux surface (inner red contour) based on a pressure model. Additionally, currents are added in the upper mirror region. Two currents (I_{M1} and I_{M2}) are evenly distributed over a finite set of points in the upper mirror.

with $g \approx 2.5$ [27]. The pressure of these plasmas were anisotropic and consisted almost entirely of an energetic electron population. When the dipole was supported, the plasma density was approximately uniform, but, when the dipole was magnetically levitated, a strong inward particle pinch was observed that results in a centrally peaked density, with an invariant power-law profile [28].

In the experiments reported here, we perform the first magnetic reconstructions of the pressure profile with the dipole magnetically levitated and find the pressure profile can be represented with a power-law model. When the dipole is magnetically levitated, equation (1) represents the pressure profile, and the thermal plasma pressure is significant, and $\beta > 10\%$. The plasma rotation is not directly measured; however, turbulent low-frequency fluctuations of density and electrostatic potential have an ensemble-averaged rotation in the electron drift direction between 1 and 3 kHz. With $\Omega/2\pi \sim 3$ kHz, $M_\Omega \approx 0.04$, and the corrections to the equilibrium plasma current are of the order of 0.1%. This small level of rotation does not effect the high pressure equilibrium reported here and was not included in results shown here.

2. Reconstructed pressure profiles

Model based reconstructions of the pressure profile in LDX are performed with measurements from 12 azimuthal flux loops and 15 poloidal field coils.

2.1. Pressure model

The pressure model used in the magnetic reconstructions has six parameters: the peak pressure parameter (p_0), the radial location of the pressure peak (R_0), the profile steepness parameter (g), the anisotropy parameter (a), and the upper mirror currents (I_{M1} and I_{M2}). The profile steepness parameter, g , expresses the outer radial power-law variation.

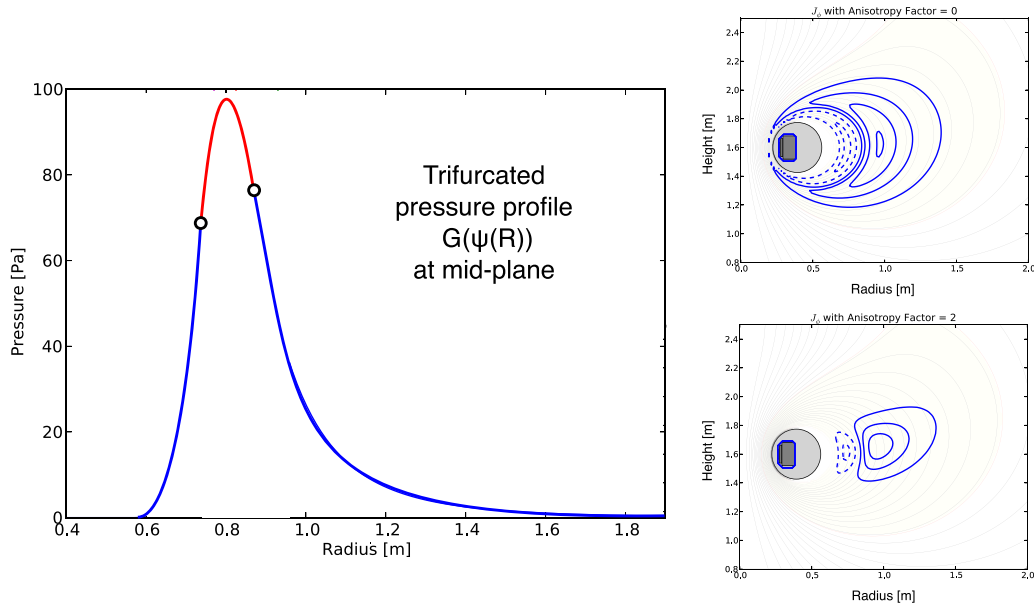


Figure 3. Left: illustration of the isotropic pressure profile, $G(\psi)$, at mid-plane. Right: illustration of the current density with an isotropic anisotropy parameter ($a = 0$, top) and an anisotropic anisotropy parameter ($a = 2$, bottom). Solid blue contours indicate a positive azimuthal current density; dashed blue contours indicate a negative azimuthal current density.

The upper mirror currents account for plasma currents in the non-confined magnetic mirror region located between the floating coil and the levitation coil, as shown in figure 2. The other model parameters set the distribution of the plasma ring current inside the dipole confinement region.

From ideal MHD, the equilibrium diamagnetic current for an anisotropic pressure is

$$\mathbf{J} = \frac{\mathbf{B} \times \nabla \cdot \bar{\mathbf{p}}}{B^2} = \frac{\mathbf{B} \times \nabla \cdot p_{\perp}}{B^2} + (p_{\parallel} - p_{\perp}) \frac{\mathbf{B} \times \boldsymbol{\kappa}}{B^2} \quad (3)$$

where $\bar{\mathbf{p}} = p_{\perp} \bar{\mathbf{I}} + (p_{\parallel} - p_{\perp}) \hat{\mathbf{b}} \hat{\mathbf{b}}$ is the pressure tensor with $\bar{\mathbf{I}}$ the identity matrix and $\hat{\mathbf{b}}$ a unit vector along the magnetic field ($\mathbf{B} = B \hat{\mathbf{b}}$), p_{\parallel} and p_{\perp} are the parallel and perpendicular components of the pressure, and $\boldsymbol{\kappa} = \hat{\mathbf{b}} \cdot \nabla \hat{\mathbf{b}}$ is the magnetic curvature. Using the vacuum field approximation of the curvature vector, $\boldsymbol{\kappa} \approx (\nabla_{\perp} B)/B$, the azimuthal component of the current density can be written in cylindrical coordinates as

$$J_{\phi} = -2\pi R \frac{\partial p_{\perp}}{\partial \psi} - 2\pi R (p_{\parallel} - p_{\perp}) \frac{\partial}{\partial \psi} (\ln B) \quad (4)$$

where R is the radial coordinate and ψ is a poloidal flux function ($\psi = RA_{\phi}$, where A_{ϕ} is the azimuthal component of the magnetic vector potential).

We parameterize the plasma pressure anisotropy by the relation $p_{\perp} = (1 + 2a)p_{\parallel}$ where a is the anisotropy parameter. Then, from parallel momentum balance [29], the perpendicular pressure [30] is modeled as

$$p_{\perp} = G(\psi) \left(\frac{B_0}{B} \right)^{2a} \quad (5)$$

where $G(\psi)$ is a flux function and B_0 is the minimum magnetic field strength along a magnetic field line.

The flux function $G(\psi)$ expresses the radial power-law dependence of the pressure and allows comparison with previous observations and studies. $G(\psi)$ is defined in three regions

$$G(\psi) = \begin{cases} p_0 \left(\frac{\psi - \psi_{\text{fcoil}}}{\psi_0 - \psi_{\text{fcoil}}} \right)^{\alpha} & , \psi > \psi_0 + \delta\psi \\ A\psi^2 + B\psi + C & , \psi_0 + \delta\psi \geq \psi > \psi_0 - \delta\psi \\ p_0 \left(\frac{\psi}{\psi_0} \right)^{4g} & , \psi \leq \psi_0 - \delta\psi \end{cases} \quad (6)$$

where $\psi_0 = \psi(R_0)$, ψ_{fcoil} is the value of ψ at the levitated dipole coil (the floating or ‘F-coil’), and $\alpha = 4g(|\psi_{\text{fcoil}}/\psi_0| - 1)$. The coefficients A , B , and C are defined such that G and $dG/d\psi$ are continuous. The width $\delta\psi$ is a fixed value that typically spans about a 5 cm radial distance at the mid-plane. Figure 3 illustrates the flux function $G(\psi)$ and the effect of the anisotropy parameter on the current density distribution. The power-law formulation of the outer pressure profile, $G(\psi) \propto \psi^{4g}$, in equation (6) is motivated by models developed to characterize plasma profiles in the Earth’s magnetosphere and used in previous research [11, 18, 22, 24, 31].

The poloidal flux function, ψ , is related to the azimuthal current by the partial differential equation

$$\Delta^* \psi = -\mu_o R J_{\phi}(\psi) \quad (7)$$

where $\Delta^* \equiv R^2 \nabla \cdot (R^{-2} \nabla)$, and μ_o is the permeability of free space. Equation (7) is iteratively solved on a grid to determine the plasma boundary and distribution of plasma currents. The reconstruction grid is shown in figure 2.

The current in the floating coil is initially determined by balancing the gravitational force on the coil with the force exerted on it by the levitation coil. At subsequent times (when there may be changes in the floating coil position, the

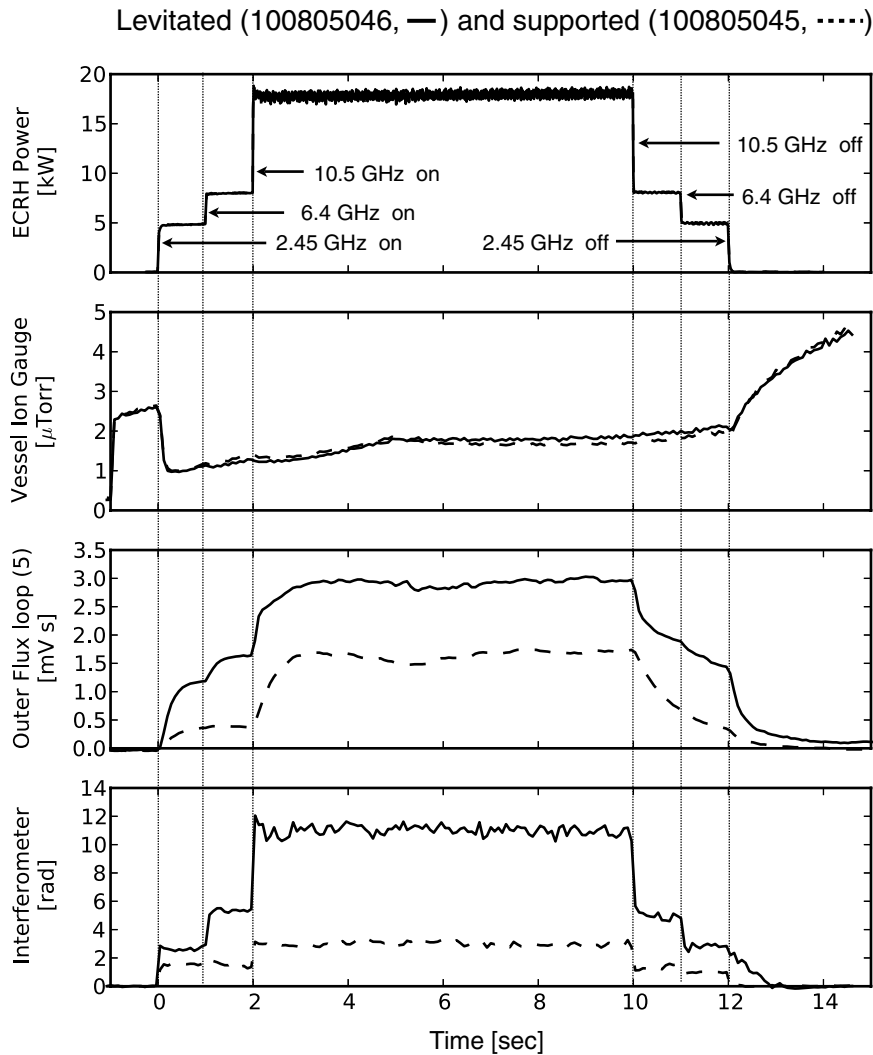


Figure 4. Overview of supported shot 100805045 (dashed lines) and levitated shot 100805046 (solid lines). The top row shows that the heating power profile was the same in both shots. The second row shows that the vessel pressure was similar on both shots. The third row shows that during levitation the change in the magnetic flux measured by a flux loop at the outer mid-plane (5 m dia.) is nearly a factor of two greater than during supported operation. The last row shows the phase measurement of the innermost chord of the interferometer (0.77 m tangency radius). The large phase change on the inner chord during levitation shows that the electron density is much higher and centrally peaked during levitated operation. The thin vertical black lines mark times when the input power changes.

levitation coil current, or the addition of plasma currents) the current in the superconducting floating coil adjusts to conserve magnetic flux.

2.2. χ^2 Model Fitting

Model parameters are determined by a nonlinear χ^2 minimization process that is described in detail in [32]. The figure of merit, χ^2 , is defined as the summation over the square deviations between the reconstructed and measured magnetic measurements (15 flux loops and 12 poloidal field coils) normalized to known measurement uncertainty variances that were calibrated by various concentric loops of known current. To determine the best fit parameters the global variation of χ^2 in the parameter space is first mapped with a parameter scan. Then, a downhill simplex method is used to home in on the best parameter fit. Estimates of the errors in the parameter values are made by propagating the known measurement errors via a Monte Carlo method [33].

3. Results

3.1. Levitated and supported plasmas

We compare a supported (100805045) and levitated (100805046) shot that have been programmed to be identical except that for the supported shot all field lines terminate on material structures and for the levitated shot field lines in the confining volume are closed. Figure 4 shows that input ECRH power and the vessel pressure are similar in both shots; however, when levitated the diamagnetic flux and plasma density are larger. We magnetically reconstruct the pressure profiles for both of these shots. Table 1 shows the best fit parameters and calculated plasma parameters for the supported and the levitated plasma. Figure 5 shows the results of this minimization and error analysis for the levitated plasma. Figure 6 illustrates the spatial distribution of the reconstructed pressure and current profiles for both the supported and levitated case.

Table 1. Pressure profile parameters and plasma parameters for magnetic reconstructions of levitated shot 100805046 and supported 100805045 with multiple ECRH sources. The global energy confinement time is the plasma energy divided by the total microwave input power.

Model Parameters	Levitated	Supported
Power (2.45, 6.4, 10.5 kHz)	18 kW	18 kW
Cord 2 line density [†]	$6.4e19 \text{ m}^{-2}$	$2.1e19 \text{ m}^{-2}$
Pressure parameter, p_0	426 Pa	2380 Pa
Pressure peak location, R_0	$0.81^\circ \pm 0.05 \text{ m}$	$0.73^\circ \pm 0.02 \text{ m}$
Profile steepness parameter, g	$2.1^\circ \pm 0.2$	7 ± 0.6
Anisotropy parameter, $a^{\dagger\dagger}$	0.5	2.0
Upper mirror inner current, I_{M1}	-1 A	-2730 A
Upper mirror outer current, I_{M2}	-155 A	-1.8 A
Resulting Plasma Parameters	Levitated	Supported
Peak pressure	268 Pa	2380 Pa
Plasma energy	250 J	278 J
Beta at pressure peak	8.6%	46%
Total plasma current	3.0 kA	2.8 kA
Plasma dipole moment	12.1 kA m^2	7.4 kA m^2
Global energy confinement	14 ms	15 ms
χ^2	19.4	35

[†] Interferometer cord with tangency radius $R = 0.86 \text{ m}$.

^{††} Parameter held fixed during χ^2 minimization.

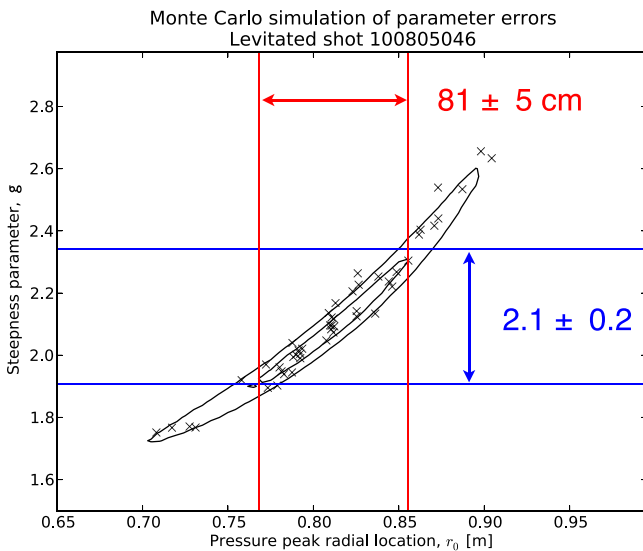


Figure 5. Monte Carlo simulation of parameter errors for levitated shot 100805046. The value of the steepness parameter is 2.1 with a standard deviation of about 0.2. The black contours mark values of constant χ^2 . The inner contour is defined by $\chi^2 = \chi_{\min}^2 + \delta\chi^2$ where $\chi_{\min}^2 = 19.4$ and $\delta\chi^2 = 0.9$.

Levitating the dipole magnet causes the pressure profile to be broader than it is during supported operation. We interpret this to be a result of eliminating losses along the field lines. This allows a more thermal plasma to develop and the pressure profile to be determined by the cross-field transport. When the dipole is in the supported mode, the pressure consists almost entirely of a mirror-trapped, energetic electron population that is created by ECRH. This hot population is known to be gyrokinetically stabilized by sufficiently dense background plasma [34, 35]. When stabilized, the pressure

profiles are observed to exceed the usual MHD stability limit shown in equation (1) [18, 27]. When the background plasma density decreases, dipole plasma with energetic electrons are unstable to the hot electron interchange mode [36, 37]. By contrast, when the dipole is in the levitated mode, the pressure consists of both an energetic electron population and a more thermal population. The presence of these two populations is observed as a fast and a slow decay time of the diamagnetic current after all the power sources have been turned off [38]. The slow decay time corresponds to the slow loss of the deeply trapped energetic electron population; the fast decay time corresponds to the rapid loss of a more thermal population. During supported mode only a single slow decay time of the diamagnetic current is observed.

The steepness of the pressure profile is quantified in the pressure model by the steepness parameter, g . Table 1 shows that for the supported plasma the steepness parameter is more than three times larger than it is for the levitated plasma. To compare pressure profiles to the marginal stability point of the MHD interchange mode we plot pV^ν as a function of radius in figure 7. For the supported plasma pV^ν decreases with radius outside of the pressure peak indicating that the pressure profile is steeper than the MHD limit. This is consistent with the supported plasma pressure consisting of an energetic electron population that is stabilized by the background plasma as discussed in the previous paragraph. For the levitated plasma pV^ν is nearly constant outside the pressure peak indicating that the pressure profile is near the marginal stability point where plasma flux-tubes can interchange position without changing the pressure profile.

The best-fit magnetic reconstructions are consistent with $a \approx 0$ for levitated plasmas where the plasma can become isotropic without particle loss. Reconstructions with a supported dipole used $a \approx 2$. For both cases, the best-fit reconstructions are not very sensitive to the anisotropy parameter, a , so the Monte-Carlo studies varied only g and R_0 .

3.2. Single frequency heating

Of the four heating ECR frequencies utilized, the low frequency source (2.45 GHz) has a resonance on the outer midplane while the higher frequencies (10.5 and 28 GHz) do not. The 6.4 GHz source has a resonance very close to the coil. As seen in figure 8, the mod-B contours of the higher frequencies are obstructed by the floating coil.

Table 2 shows results from a series of equilibrium calculations for single source heating discharges. We observe that adding power at low frequencies which have an outer midplane resonance (2.45 GHz) tends to produce run away electrons and to produce relatively low density plasmas. These plasmas have relatively peaked pressure profiles with the pressure peak located at the midplane resonance. Heating at the higher frequencies (10.5 and 28 GHz), such that there is no midplane fundamental resonance, tends to produce higher density plasmas. The hot electron component that accounts for the pressure consists of very peaked mirror trapped plasmas with the pressure peak located close to the innermost flux tube ($R_0 \sim 0.65 \text{ m}$) which touches the floating coil in the

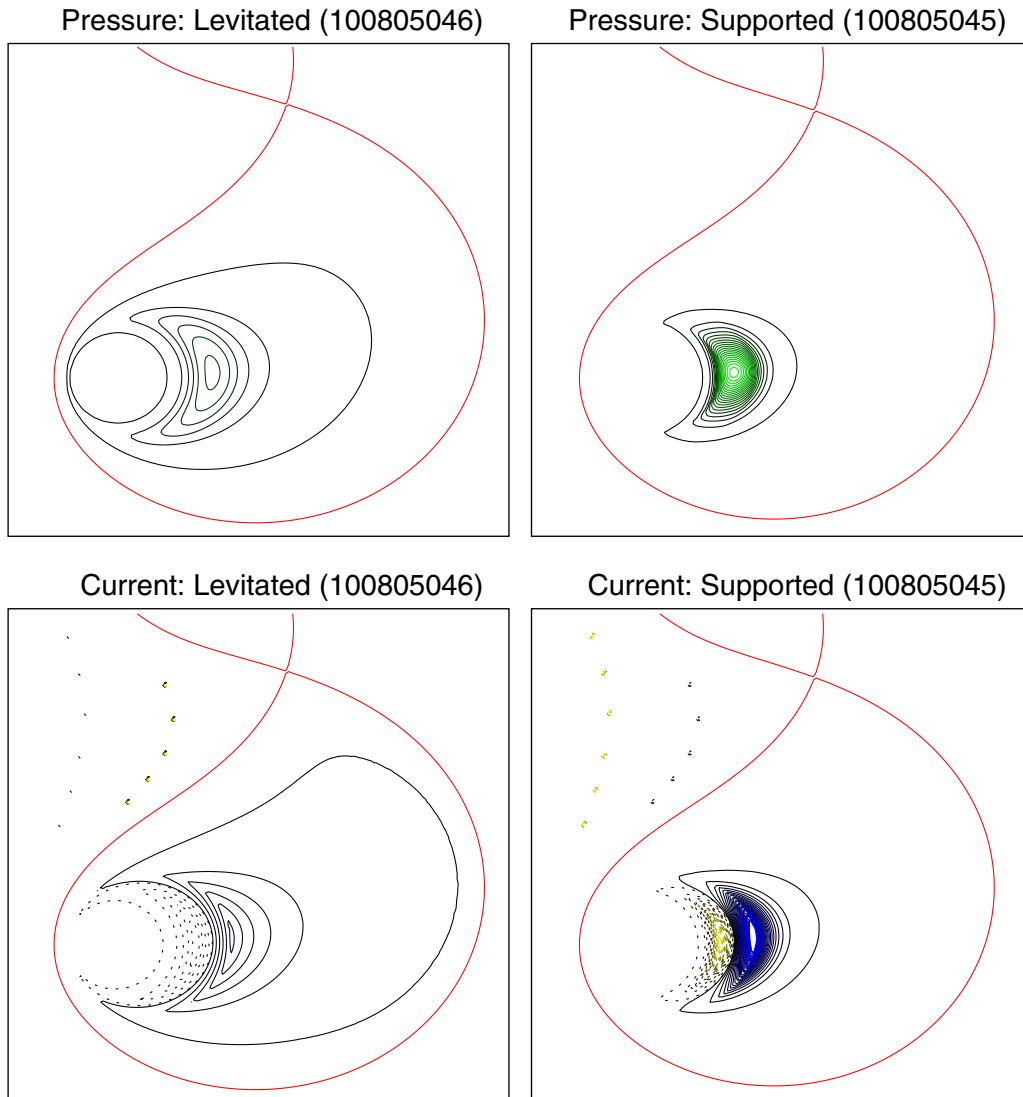


Figure 6. Pressure and current density contours for a supported (100805045) and a levitated (100805046) shot. In the top figures the pressure is shown with green contours indicating higher pressure and black contours indicating lower pressure (the same pressure contour levels are plotted for levitated and supported operation). The bottom figures show the current density with solid blue indicating high positive current density, solid black low positive current density, dotted black low negative current density, and dotted yellow high negative current density (the same current density contour levels are plotted in levitated and supported operation). The red contour marks the separatrix. During levitation the pressure and current density profiles are broader with lower maximum values.

inner radius. For the high frequencies the mod-B resonance surface cuts across all field lines, and appear to be efficient in creating density in combination with low frequency (2.45 GHz) heating.

3.3. Elimination of upper mirror currents

The plasma that forms in the mirror wells on open field lines between the floating coil and the levitation coil (see figures 2 and 8) absorbs heating power and distorts the equilibrium. Indeed, we only became aware of the presence of mirror-trapped plasma on open field lines as a consequence of the equilibrium reconstructions and after observations of visible light emission from careful videography. We eliminated the currents from mirror-trapped plasma in LDX by locating a series of rods (the ‘spider’) that intercept the plasma that tends to form in this region. Without the ‘spider’,

the best fit equilibria *required* the presence of diamagnetic currents from mirror-trapped plasma. After the ‘spider’ was installed, the best fit equilibria had very small or zero diamagnetic currents from electrons mirror-trapped on open field lines. Furthermore, after the ‘spider’ was installed, plasma light from the mirror-trapped, open field-line region became unobservable. We saw no evidence of surface heating from the ‘spider’, and there was no build-up of electron pressure that might enhance microwave absorption.

Table 3 compares levitated shots with similar ECR heating power and neutral gas pressure. Discharge 100527002 permits upper mirror currents to form whereas in 130814045 the spider largely eliminates these currents. We have magnetically reconstructed the equilibrium for both of these shots. Table 3 shows the best fit parameters and calculated plasma parameters for the plasma with and without mirror plasma. The equilibria

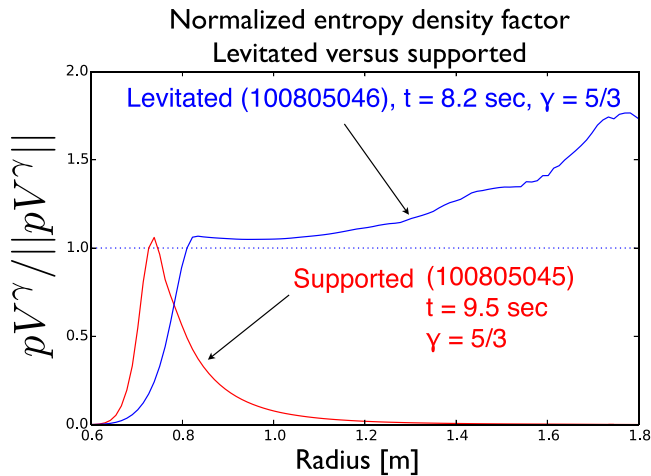


Figure 7. For levitated shot 100805046 with multiple ECRH sources on the entropy density factor is constant with radius outside the pressure peak (at radius 81 cm). This is consistent with a pressure profile that is marginally stable to the MHD interchange mode. For supported shot 100805045 with multiple ECRH sources on the entropy density factor decreases with radius outside the pressure peak (at radius 73 cm) indicating a pressure profile that is steeper than the MHD limit.

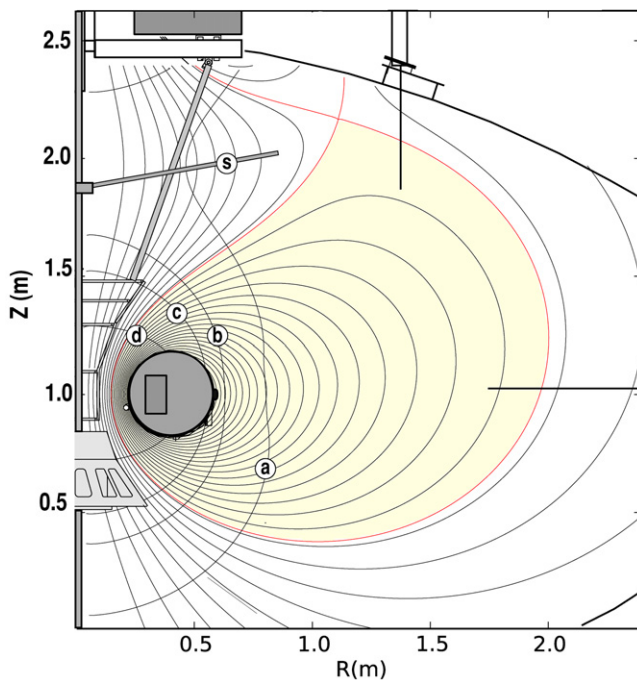


Figure 8. Flux plot for high power (27 kW) heating (130814045) showing mod-B contours corresponding to resonances that cross the midplane ($Z = 1$ m) at (a) $R = 0.80$ m (2.45 GHz), (b) $R = 0.62$ m (6.4 GHz), (c) $R = 0.55$ m (10.5 GHz), and (d) $R = 0.44$ m (28 GHz). The unconfined, mirror trapped plasma is located near $Z \sim 2$ m, $R \sim 0.2$ –1 m and is largely eliminated by the ‘spider’ (s).

indicates the near elimination of mirror currents and in particular a substantial drop in I_{m2} .

Furthermore, line density rises by 50% when the mirror plasma is eliminated. In the absence of mirror trapped plasma it is likely that a larger fraction of the heating power goes into the plasma confined on closed field lines. Consistent with

Table 2. Plasma parameters for magnetic reconstructions of single heating source discharges 130814023 (2.45 GHz), 130814020 (10.5 GHz) and 130814016 (28 GHz) respectively.

	2.45 GHz	10.5 GHz	28 GHz
Heating frequency	2.45 GHz	10.5 GHz	28 GHz
Power	5.1 kW	10 kW	10 kW
Cord 2 line density [†]	$1.1e19$ m ⁻²	$4.2e19$ m ⁻²	$4.9e19$ m ⁻²
Peak pressure, p_0	38.1 Pa	435 Pa	105 Pa
Radius of peak, R_0	0.80 m	0.65 m	0.65 m
$B(R_0)$	0.096 T	0.197 T	0.199 T
Steepness param, g	2.0	3.47	2.6
Anisotropy param, $a^{\dagger\dagger}$	0.5	0.5	0.5
Inner current, I_{M1}	-8.2 A	-1.0 A	-1.0
Outer current, I_{M2}	-1.0 A	-14.2 A	-8.8 A
Resulting Plasma			
Plasma energy	28 J	79 J	25 J
Beta at pressure peak	1.0%	2.8%	0.67%
Total plasma current	0.31 kA	0.62 kA	0.21 kA
Plasma dipole moment	1.30 kA m ²	1.17 kA m ²	.47 kA m ²

[†] Interferometer cord with tangency radius $R = 0.86$ m.

^{††} Anisotropy parameter held fixed during χ^2 minimization.

Table 3. Pressure profile parameters and plasma parameters for magnetic reconstructions of levitated shots 100527002 (without spider) and 130805045 (with spider) at $t = 6$ s with multiple ECRH heating sources (27 kW total).

Measured Parameters (t=6s)	no spider	spider
Ion gauge pressure	3×10^{-6} torr	2.8×10^{-6} torr
Cord 2 line density	9×10^{18} m ⁻²	15×10^{18} m ⁻²
Model Parameters	with I_M	without I_M
Peak Pressure, p_0	748 Pa	497 Pa
Radius of peak, R_0	0.78 m	0.83 m
$B(R_0)$	0.091 T	0.075 T
Profile steepness parameter, g	2.5	2.4
Anisotropy parameter, a	0.5^{\dagger}	0.5^{\dagger}
Upper mirror inner current, I_{M1}	-1.2 A	-2.4 A
Upper mirror outer current, I_{M2}	-206 A	-1.0 A
Resulting Plasma Parameters	with I_M	without I_M
Plasma energy	392 J	336 J
Beta at pressure peak	23%	22%
Total plasma current	4.3 kA	3.9 kA
Plasma dipole moment	15.1 kA m ²	15.9 kA m ²
Global energy confinement	14.5 ms	12.4 ms

[†] Parameter held fixed during χ^2 minimization.

the previous observations, we expect that the plasma density rises proportional to injected power [39]. However, the energy stored in the hot electron species is known to fall with rising density which would account for the small drop in stored energy, even as we expect that the energy in the background thermal plasma rises. Other parameters (β , dipole moment, total current), do not change significantly.

4. X-ray measurements

X-ray emission is measured with a silicon drift detector (2–20 keV) and cadmium zinc telluride (CZT) detectors (10–650 keV). The spectra from supported and levitated

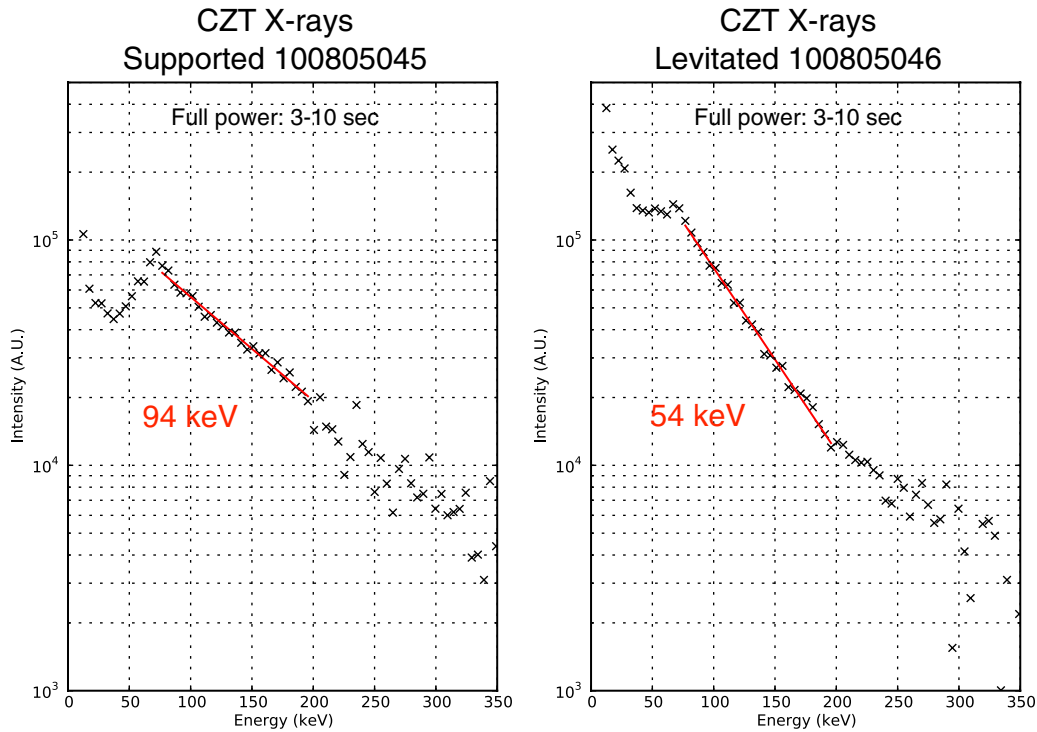


Figure 9. Spectra from CZT detectors with view tangency radius 113 cm for supported and levitated plasmas. Spectra are corrected for the transmission efficiency and sensitivity of the CZT detectors.

plasmas show that the observed x-rays come from a minority energetic electron population that can be described with a log-linear energy distribution in the range 50–100 keV (see figure 9). Although the peak density of the levitated plasma is an order of magnitude greater than peak density of the supported plasma the intensity of the levitated spectra is similar to the supported spectra indicating that the minority energetic electron population is smaller for levitated plasmas.

An estimate of the hot electron peak density is made by dividing the peak pressure determined from the magnetic reconstruction by the pseudo-temperature of the energetic electron population determined from the x-ray spectra. An upper bound estimate of the hot electron fraction (n_{HOT}/n_e) is made by dividing the hot electron density (n_{HOT}) by the total density (n_e) measured by the interferometer. For this estimate it is assumed that all the pressure is in the hot electrons.

In the supported plasma case (100805045) this assumption is supported by the measurement of a single slow decay time of the diamagnetism after the power is shut off [38]. Thermal plasma is rapidly lost to the mechanical supports and all the plasma pressure is contained in the hot electron population. The maximum hot electron fraction at the pressure peak is $\sim 75\%$ for the supported plasma.

In the levitated case (100805046) the maximum hot electron fraction is $\sim 3.5\%$; however, this must be an overestimate because the assumption that all the pressure is in the hot population can not be valid. For the levitated plasma, both a fast and a slow decay time of the diamagnetism are observed after the power is shutoff indicating the pressure is composed of both a hot population and a more thermal population [38]. Furthermore, the higher density plasma with a levitated dipole generates an x-ray emission that is comparable

in intensity to that observed with a supported dipole even with an order of magnitude less plasma density. This indicates a smaller density of energetic electrons scattering from a higher plasma density generates an x-ray signal similar to the higher density of energetic electrons scattering from the lower plasma density found with a supported dipole. Thus, the comparable intensity of measured x-ray (figure 9) implies the levitated discharge has a hot electron fraction, $n_{\text{HOT}}/n \approx 1\%$, which significantly reduced from the much lower density discharge obtained using a supported dipole. As expected, levitation eliminates losses to the mechanical supports allowing a thermal plasma to form.

Finally, it is generally found that shots with fewer x-rays have broader magnetically reconstructed pressure profiles.

5. Summary

We report magnetic reconstructions of the pressure profile for dipole confined plasmas for which the dipole was magnetically levitated. Levitated plasmas adopt pressure profiles that are broader than the profiles observed during supported operation. The resulting profiles have both density and pressure profiles that are centrally peaked and that have radial gradients nearly stationary to convective interchange mixing. Our experiments show that peaked density profiles with $\delta(nV) \sim 0$ and peaked pressure profiles with $\delta(pV\gamma) \sim 0$ can now be produced routinely in the laboratory in essentially steady-state conditions and at high plasma beta. This demonstration shows a key connection between the physics of magnetospheric plasma and the physics of plasma confined in the laboratory.

We hypothesize that these profiles occur ‘naturally’ as a result of turbulent self-organization. These peaked profiles

are the ‘canonical’ profiles that minimize entropy production during low-frequency turbulence as described, for example, in [22, 23]. These profiles also represent stationary states of space-weather dynamics, as described, for example, in [20], when driven mixing of magnetospheric plasma does not alter plasma profiles.

Investigations with various combinations of applied microwave heating have allowed a better understanding of the influence of the location of cyclotron resonance in LDX. With single frequency heating the pressure peak appears to be located at the outer midplane resonance when there is a midplane fundamental resonance such as with heating at 2.45 GHz. In the absence of an outer midplane fundamental resonance (i.e. when microwave heating is applied only with frequencies > 6 GHz) the pressure of energetic electrons peaks on the innermost field line that closes around the floating coil. Furthermore, we have observed that a mirror trapped plasma tends to form in the unconfined region above the floating coil. When a spider-like structure is utilized to intercept this upper mirror-trapped plasma, we observe the plasma line-density of the dipole-confined plasma to increase significantly ($> 50\%$).

Our next step research involves three areas. First, we plan to make direct measurements of the electron temperature and density profiles through Thomson scattering. Second, we will conduct controlled laboratory investigations of plasmas having higher density (with $c/\omega_{pi}L \ll 1$) and higher ion temperature ($T_i \sim T_e$) by operating our high-power RF heating system. This would allow systematic study of ion gyrokinetics under the influence of interchange/entropy modes and the study of Alfvén dynamics in a large laboratory magnetosphere. Finally, the large, steady-state plasmas produced in laboratory magnetospheres provide opportunities to conduct controlled experimental investigations of transient phenomena that result, for example, from launching particle, plasma, and magnetic field perturbations.

Acknowledgments

We acknowledge research funding from the NSF/DOE Partnership in Plasma Science, US DOE Grant DE-FG02-00ER54585 and NSF Award PHY-1201896 and several valuable suggestions from the referees.

References

- [1] Daglis I 1999 *Rev. Geophys.* **37** 407
 [2] Lyon J 2000 *Science* **288** 1987
 [3] Jorgensen A 2004 *J. Geophys. Res.* **109** A12204

- [4] Russell C and Huddleston D 1997 *Adv. Space Res.* **20** 327
 [5] Stepanova M 2006 *Adv. Space Res.* **38** 1631
 [6] Krimigis S 2007 *Nature* **450** 1050
 [7] Hasegawa A 1987 *Comments Plasma Phys. Control. Fusion* **11** 147
 [8] Hasegawa A, Chen L and Mauel M 1990 *Nucl. Fusion* **30** 2405
 [9] Kesner J and Mauel M 1997 *Plasma Phys. Rep.* **23** 742
 [10] Kesner J, Garnier D, Hansen A, Mauel M and Bromberg L 2004 *Nucl. Fusion* **44** 193
 [11] Gold T 1959 *J. Geophys. Res.* **64** 1219
 [12] Melrose D 1967 *Planet. Space Sci.* **15** 381
 [13] Fälthammar C-G 1965 *J. Geophys. Res.* **70** 2503
 [14] Birmingham T 1969 *J. Geophys. Res. Space Phys.* **74** 2169
 [15] Baker D 2001 *J. Atmos. Sol.-Terr. Phys.* **63** 421
 [16] Garnier D *et al* 2006 *Fusion Eng. Des.* **81** 2371
 [17] Garnier D, Hansen A, Mauel M, Ortiz E, Boxer A, Ellsworth J, Karim I, Kesner J, Mahar S and Roach A 2006 *Phys. Plasmas* **13** 56111
 [18] Garnier D, Kesner J and Mauel M 1999 *Phys. Plasmas* **6** 3431
 [19] Rosenbluth M and Longmire C 1957 *Ann. Phys.* **1** 120
 [20] Toffoletto F, Sazykin S, Spiro R and Wolf R 2003 *Space Sci. Rev.* **107** 175
 [21] Kobayashi S and Rogers B 2009 *Phys. Rev. Lett.* **103** 055003
 [22] Kesner J, Garnier D and Mauel M 2011 *Phys. Plasmas* **18** 050703
 [23] Garbet X 2005 *Phys Plasmas* **12** 082511
 [24] Krasheninnikov S, Catto P and Hazeltine R 1999 *Phys. Rev. Lett.* **82** 2689
 [25] Lui A and Hamilton D 1992 *J. Geophys. Res.* **97** 19325
 [26] Chen M, Lyons L and Schulz M 1994 *J. Geophys. Res.* **99** 574505759
 [27] Karim I, Mauel M E, Ellsworth J L, Boxer A C, Garnier D T, Hansen A K, Kesner J and Ortiz E E 2007 *J. Fusion Energy* **26** 99
 [28] Boxer A, Bergmann R, Ellsworth J, Garnier D, Kesner J, Mauel M, and Woskov P 2010 *Nature Phys.* **6** 207
 [29] Connor J and Hastie R 1976 *Phys. Fluids* **19** 1727
 [30] Krasheninnikov S and Catto P 2000 *Phys. Plasmas* **7** 626
 [31] Walt M 1971 *Space Sci. Rev.* **12** 446
 [32] Davis M 2013 Pressure profiles of plasmas confined in the field of a dipole magnet *PhD Thesis* Columbia University, New York, NY
 [33] Press W, Flannery B, Teukolsky S and Vetterling W 1989 *Numerical Recipes in Pascal: The Art of Scientific Computing* (Cambridge: Cambridge University Press)
 [34] Krall N 1966 *Phys. Fluids* **9** 820
 [35] Berk H 1976 *Phys. Fluids* **19** 1255
 [36] Levitt B, Maslovsky D and Mauel M 2002 *Phys. Plasmas* **9** 2507
 [37] Ortiz E, Boxer A, Ellsworth J, Garnier D, Hansen A, Karim I, Kesner J and Mauel M 2007 *J. Fusion Energy* **26** 139
 [38] Garnier D, Boxer A, Ellsworth J, Kesner J and Mauel M 2009 *Nucl. Fusion* **49** 055023
 [39] Kesner J, Davis M, Ellsworth J, Garnier D, Mauel M, Michael P, Wilson B and Woskov P 2010 *Plasma Phys. Control. Fusion* **52** 124036